

# Enhanced *In Vivo* Bone and Blood Vessel Formation by Iron Oxide and Silica Doped 3D Printed Tricalcium Phosphate Scaffolds

SUSMITA BOSE, DISHARY BANERJEE , SAMUEL ROBERTSON, and SAHAR VAHABZADEH

Washington State University, Pullman, WA 99164-2920, USA

(Received 1 February 2018; accepted 26 April 2018; published online 4 May 2018)

Associate Editor Michael S. Detamore oversaw the review of this article.

**Abstract**—Calcium phosphate (CaP) ceramics show significant promise towards bone graft applications because of the compositional similarity to inorganic materials of bone. With 3D printing, it is possible to create ceramic implants that closely mimic the geometry of human bone and can be custom-designed for unusual injuries or anatomical sites. The objective of the study was to optimize the 3D-printing parameters for the fabrication of scaffolds, with complex geometry, made from synthesized tricalcium phosphate (TCP) powder. This study was also intended to elucidate the mechanical and biological effects of the addition of  $\text{Fe}^{+3}$  and  $\text{Si}^{+4}$  in TCP implants in a rat distal femur model for 4, 8, and 12 weeks. Doped with  $\text{Fe}^{+3}$  and  $\text{Si}^{+4}$  TCP scaffolds with 3D interconnected channels were fabricated to provide channels for micronutrients delivery and improved cell-material interactions through bioactive fixation. Addition of  $\text{Fe}^{+3}$  into TCP enhanced early-stage new bone formation by increasing type I collagen production. Neovascularization was observed in the  $\text{Si}^{+4}$  doped samples after 12 weeks. These findings emphasize that the additive manufacturing of scaffolds with complex geometry from synthesized ceramic powder with modified chemistry is feasible and may serve as a potential candidate to introduce angiogenic and osteogenic properties to CaPs, leading to accelerated bone defect healing.

**Keywords**—3D printing, Porous scaffold, Interconnected porosity, Tricalcium phosphate, *In vivo* behavior, Osteogenesis and angiogenesis, Accelerated bone defect healing.

## INTRODUCTION

Autografts are still considered the gold standard for bone tissue regeneration; however, their availability is often limited by the finite amount of donor tissue from one surgical site and a second surgical site may be necessary.<sup>3,11</sup> CaP based ceramics, like hydroxyapatite

(Hap,  $\text{Ca}_{10}(\text{PO}_4)_6(\text{OH})_2$ ) and  $\beta$ -TCP ( $\beta\text{-Ca}_3(\text{PO}_4)_2$ ), have found ample use in tissue engineering scaffolds for their compositional similarity to natural bone.<sup>4,30</sup> Unlike Hap,  $\beta$ -TCP is resorbed by the body at a rate similar to the regeneration rate of bone.<sup>30</sup> This time-dependent dissolution of  $\beta$ -TCP provides temporary mechanical support for injured bone until it is eventually replaced by the natural tissue and thus, are used widely for craniomaxillofacial applications.<sup>15,27</sup>

Since natural bone is porous with interconnected porosity, the tissue engineering community has endeavored to fabricate porous scaffolds with interconnected porosity. Interconnected pores within a scaffold promote cell adhesion, enhances bone formation and thereby promotes biological fixation at the implant–bone interface.<sup>5,32,33</sup> They also prove to be beneficial in the initiation of blood vessel formation by facilitating the removal of metabolic waste products from the scaffold and allowing a flow of blood and nutrients into the core of the scaffold,<sup>8,13,29</sup> which is crucial for the functional activities of any tissue. The consensus on the optimal pore size to allow osteogenesis is approximately 300–500  $\mu\text{m}$  in diameter<sup>16</sup> which is comparable to the optimal pore diameter for angiogenesis.<sup>25</sup>

Fabrication of CaP scaffolds with complexly interconnected porosity using conventional manufacturing techniques is grueling because of the precision needed over the pore sizes, pore diameter, interconnectivity amongst the pores, pore size distribution and volume fraction porosity. Our previous works have reported the use of a powder bed 3D printing technique to fabricate complex geometries with interconnected porosity out of commercial Berkley CaP powders.<sup>8,30</sup> This study intends to fabricate scaffolds out of TCP, synthesized by the solid-state method in the laboratory, with interconnected porosity and precisely con-

Address correspondence to Susmita Bose, Washington State University, Pullman, WA 99164-2920, USA. Electronic mail: sbose@wsu.edu

trolled designed pore sizes for the induction of osteogenesis and angiogenesis properties.

Furthermore, the inorganic portion of the bone is not pure HA, but rather carbonated HA (CHA). In CHA, each of the functional groups can be exchanged for a variety of ions or groups like  $\text{Mg}^{+2}$ ,  $\text{Sr}^{+2}$ ,  $\text{Na}^{+}$ ,  $\text{Zn}^{+2}$ ,  $\text{Si}^{+4}$ ,  $\text{Fe}^{+3}$  for  $\text{Ca}^{+2}$ ,  $\text{CO}_3^{2-}$  for  $\text{PO}_4^{-3}$  and  $\text{F}^{-}$  for  $\text{OH}^{-}$ . Our previous works<sup>2,7,31</sup> have shown the incorporation of a variety of dopants into CaPs and improvement of mechanical and biological properties *in vitro* and *in vivo*, without affecting the inherent biocompatibility of commercial  $\beta$ -TCP. By itself,  $\beta$ -TCP inherently triggers new bone formation on the implant surface *via* recruitment of existing osteoblasts (osteoconductivity); however, it does not promote osteoinductivity: the recruitment of stem cells and proteins to induce differentiation into pre-osteoblasts. Osteoinductivity has been previously reported in  $\beta$ -TCP by the addition of a variety of osteogenic drugs, bioactive proteins, and growth factors.<sup>4,33</sup> The introduction of cationic dopants in  $\beta$ -TCP is hypothesized to result in osteoinduction, without the need for hormones, proteins, or drugs.<sup>2,7</sup>

The human body consists of about 3.9–5 g of iron which is crucial for the daily activity of the body and is distributed throughout the body including in the bone marrow and hemoglobin.<sup>9</sup> Iron deficiency has been reported to affect the collagen maturation and vitamin D metabolism<sup>17,21</sup> and therefore, cause abnormal bone remodeling.<sup>18,22</sup> Although multiple studies of the effects of dietary iron are reported for collagen maturation and bone formation,<sup>17,18</sup> no reports, to the best of our knowledge, have been found on the incorporation of iron oxide in CaP matrix for targeted delivery *in vivo*. Previous work by our group has shown the effects of iron on new bone formation *in vitro*.<sup>31</sup> Synthesis and structural stabilization of collagen is also influenced by silicon intake.<sup>14</sup> The association between silicon intake and higher bone density argues the necessity of silicon in the human body for improved bone health.<sup>26</sup> Other studies have reported enhanced angiogenesis in 0.5 wt% silicon doped CaP scaffolds *in vivo* in a rat distal femur model.<sup>8</sup>

The considerable evidence from a variety of literature sources and, from our previous works led us to investigate the combined effects of  $\text{Si}^{+4}$  and  $\text{Fe}^{+3}$  dopants in 3D printed interconnected porous  $\beta$ -TCP scaffolds on the mechanical and biological properties *in vivo* in a rat distal femur model. None of our earlier works have examined the combined effects of  $\text{Fe}^{+3}$  and  $\text{Si}^{+4}$  on *in vivo* osteogenesis, collagen maturation, and angiogenesis. We hypothesized that the incorpo-

ration of Fe and Si would affect the compressive strengths and improve *in vivo* osseointegration and bone formation along with neovascularization. In this study, we have augmented the intrinsic osteoconductive properties of  $\beta$ -TCP were enhanced by osteoinductivity promoted through the incorporation of  $\text{Fe}^{+3}$  and  $\text{Si}^{+4}$ . The osseointegration properties of the scaffolds were further enhanced by the 3D printed, porous, interconnected complex geometry. Scaffolds were implanted into a rat femoral defect model and studied over the course of 12 weeks for osteogenic and angiogenic properties.

## MATERIALS AND METHODS

### *Powder Synthesis for Scaffold Fabrication*

Pure and Fe–Si doped  $\beta$ -TCP powder were synthesized by solid-state synthesis method as discussed in previous work.<sup>31</sup> High purity iron oxide ( $\text{Fe}_2\text{O}_3$ , < 50 nm, Sigma-Aldrich) was added to the precursors prior to milling to attain 0.5 mol%  $\text{Fe}^{+2}$  TCP.<sup>31</sup> Henceforth, this powder was represented as Fe-TCP. Similarly, Fe–Si-TCP powder was prepared by adding 0.5 wt%  $\text{SiO}_2$  (Sigma-Aldrich) to Fe-TCP powder prior to milling. Each composition was further milled for 6 h and the milled powders were eventually dried at 70 °C for 72 h.

### *Scaffold Fabrication*

The synthesized powders were used in a binder-jet printer (ProMetal<sup>®</sup>, ExOne LLC, Irwin, PA, USA) for the scaffold fabrication. Cylindrical scaffolds were designed 3 mm in diameter by 5 mm in height with 400  $\mu\text{m}$  designed interconnected pores throughout. The interconnected macropores were designed square in shape and were distributed orthogonally across the cylindrical walls.

The printing process was optimized for the synthesized powders to minimize defects. An initial 5–6 mm thick layer of foundation was deposited in the build box as a starting layer, each subsequent layer thickness was 35  $\mu\text{m}$  for pure  $\beta$ -TCP and 30  $\mu\text{m}$  for doped  $\beta$ -TCP powders. After fabrication, the scaffolds were maintained at 175 °C for 1.5 h to cure the binder and form green ceramic parts. Post-cure, the loose powder was removed with compressed air and the green parts were sintered in a muffle furnace at 1250 °C for 2 h. Scaffolds with similarly designed macropores, 6.9 mm in diameter and 10.9 mm in height were fabricated for mechanical strength analysis in accordance with ASTM C773-88 standards.<sup>1</sup> Figure 1 shows a sche-

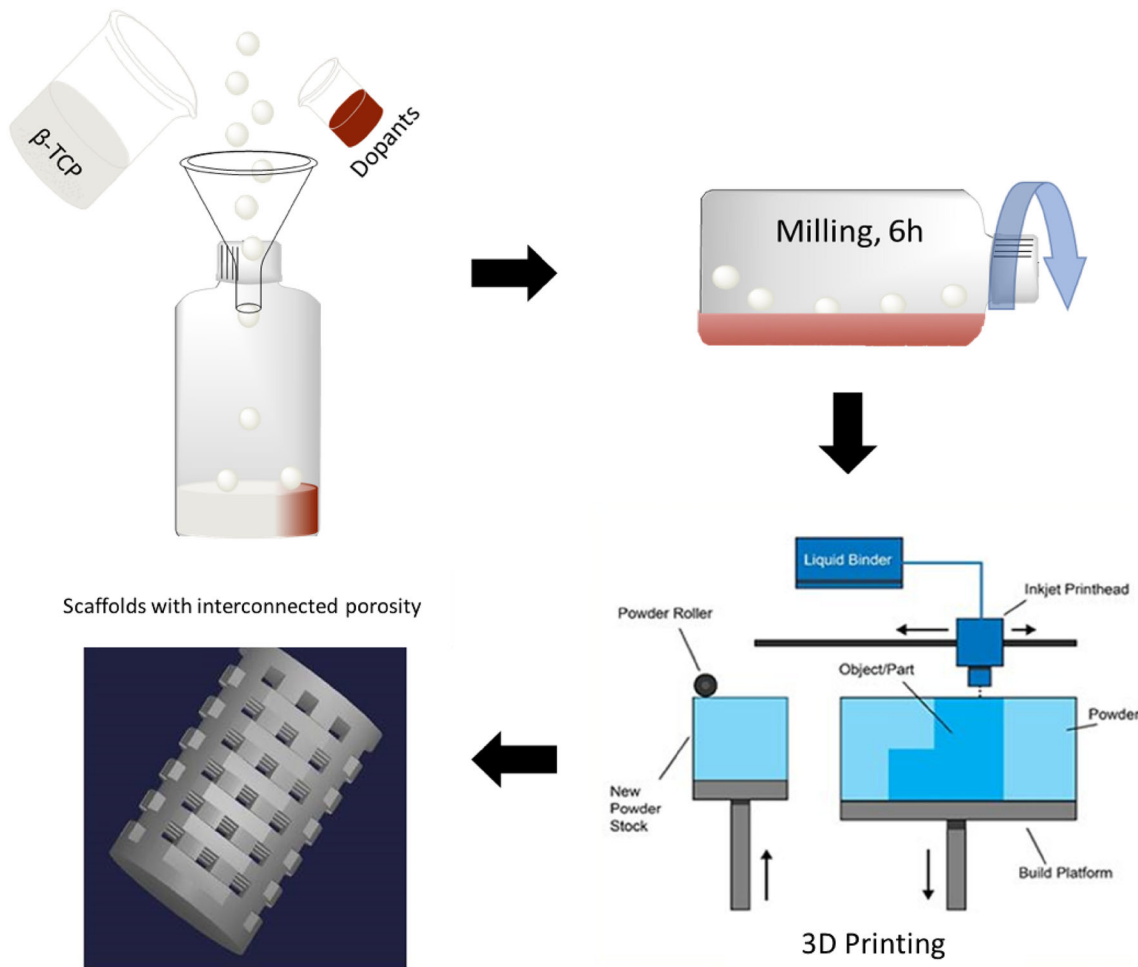


**FIGURE 1.** Schematic of doped and control scaffold preparation by 3D printing powder bed process. Scaffolds with  $400\ \mu\text{m}$  designed interconnected porosity were fabricated for implantation in rat distal femur models.

matic of the process carried out for the 3D printing of the doped powder.

### *In Vivo Study*

#### *Surgery and Implantation Procedure*

All experimental and surgery procedures were performed in accordance with Institutional Animal Care and Use Committee (IACUC) protocol authorized by Washington State University, Pullman, WA. 24 skeletally mature male Sprague–Dawley rats each about 300–350 g in weight (Envigo, Wilmington, MA, USA) were euthanized at 4, 8 and 12-week time points post-surgery using an overdose of  $\text{CO}_2$ , and the femurs were removed and preserved in 10% neutral buffered formalin solution for tissue preservation. A schematic of the intramedullary cortical defect is shown in Fig. 2.

### *Histomorphology*

Two samples for each time point and composition were dehydrated through a graded alcohol series, and embedded in Spurs resin. Cross-sections of around  $200\ \mu\text{m}$  were cut out perpendicular to the implant surface using a low-speed diamond saw and then stained with Modified Masson–Goldner trichrome staining to observe new bone formation around the area of implantation. The other samples were preserved in 14% EDTA (changed every alternate day) solution for 12 weeks for the process of decalcification. After the osseous tissue was removed, the sample was embedded in paraffin, cut into thin sections of  $10$ – $20\ \mu\text{m}$  using a microtome cutter, and put on to positively charged slides. These slides were used for Hematoxylin and Eosin (H&E) staining, collagen staining, and vWF staining to evaluate osteogenic and angiogenic property.

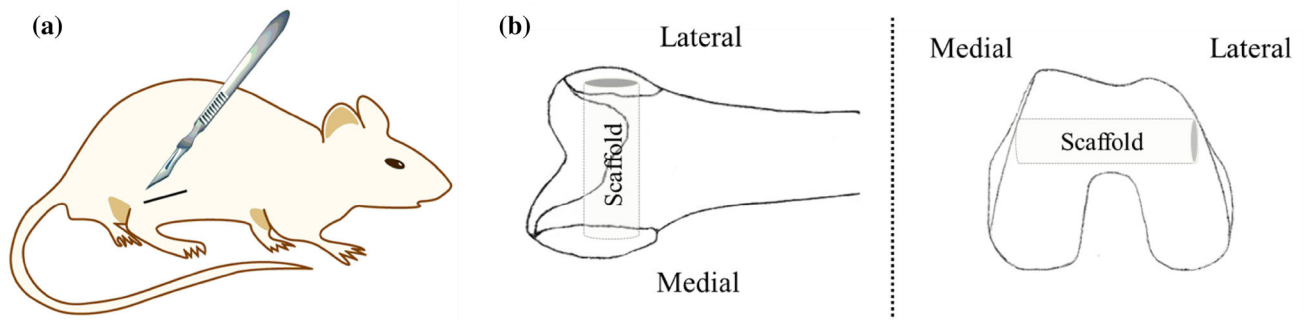


**FIGURE 2.** Surgical site (a) and the orientation of the scaffold within the femoral head (b).

Fifteen slides were used per assay, deparaffinized prior to staining, stained, and then imaged under a light microscope. vWF staining was carried out using a blood vessel staining kit (ECM 590, Millipore, MA, USA). Briefly, Rabbit anti-vWF polyclonal antibody, diluted 1:200 in phosphate buffered saline (PBS) was used as primary antibody and incubated for 2 h in a dark chamber, while ready to use goat anti-rabbit antibody (EMD Millipore, MA, USA) was used as a secondary antibody. Antigen retrieval was carried out using a steamer at 60 °C using phosphate buffer solution (pH 7.4). Hematoxylin staining was used as a counter stain for better visibility. For collagen staining, anti-rat type I collagen antibody, clone 1F10C2, biotinylated, 1 mg/mL  $\times$  0.1 mL (Chondrex, WA, USA), diluted 1:100 in PBS was used as the primary antibody for collagen staining with an incubation time of 1.5 h in an enclosed container. H&E staining was performed by emersion of the slides in Eosin reagent followed by hematoxylin counterstaining.

#### *Histomorphometric Analysis*

Image J software was utilized for analyzing the new bone formation around the implantation area. Three optical microscope images from each rat, totaling nine images at each time point and each treatment group were used for the histomorphometric analysis for statistical relevance. The bone area was analyzed from images, 1 mm by 1 mm and the percentage of the new bone formation was calculated by the ratio of the total desired bone area (reddish orange in color) normalized over the total bone formed area.

#### *Statistical Analysis*

All the data, including the histomorphometric analysis, compressive mechanical strengths of scaffolds demonstrated in this study was reported as the mean  $\pm$  standard deviation. The statistical analysis was performed by two-way ANOVA models and  $p$  values  $<$  0.05 were marked as significant.

## RESULTS

### *Density, Pore Size, Microstructure, Phase and Mechanical Strength*

Powder packing density of synthesized TCP powder was 37%. Binder drop volume was in the range of 68–70 pL at all times. Based on the powder packing density and, binder drop volume, the saturation of 92% was computed. Computed binder saturation was calculated using the Prometal Software and depended on binder drop volume, powder packing density, and layer thickness. According to the computed saturation, the desired saturation was determined as 92% at a layer thickness of 20  $\mu$ m. With initial drying of 15 s at a power of 35% and the roller speed of 0.5 mm/s, significant layer displacement occurred in the Y printing direction. Regarding the degree of displacement, the saturation was decreased to 84, 78, and 72; however, the displacement was still apparent. Layer displacement was related to the stability of the build layer during the powder spreading and binder spraying and occurred due to high binder saturation and lack of drying. In addition, excessive binder spreading along the thin layers resulted in the penetration of the binder into the powder bed and decreased the resolution of the parts.<sup>30</sup> This proved the dependency of desired saturation on parameters such as drying time and power. To decrease the layer displacement, the drying power and layer thickness were increased to 45% and 30  $\mu$ m, respectively; however, small cracks were formed on build layers after printing of few layers. Decreasing the drying time to 5 s resulted in continued crack formation and layer displacement at desired saturations of 65 and 70%. No layer displacement was found in build the layer when saturation was decreased to 50% and drying was removed; however, slight bumps and cracks was found, and the integrity of part was poor. As a result, binder saturation increased to 70%, drying time after each layer was 5 s, and the drying power increased from 35 to 55 and 70%. Increase in drying power prevents the binder spreading



between the layers and as a result, the layer displacement found in powers of 35 and 55% completely disappeared and parts with no displacement and cracks were achieved. Higher power of 80% caused the peeling off in build layers. The final running parameters for smaller porous parts was 70% of binder saturation and drying power, 5 s of drying after printing each layer with a thickness of 30  $\mu\text{m}$ . These parameters are comparable with the previous data presented from our group where a commercial Berkeley powder with similar composition was successfully printed with 110% binder saturation, a layer thickness of 25  $\mu\text{m}$  and drying power of 35%.<sup>29</sup>

Despite optimization, poor handle-ability of the parts during depowderizing caused the struts to break. Depowderization or loose powder removal from designed pores of the complex structure, is considered as one of the main disadvantages of ink-jet 3DP.<sup>19</sup> It is a critical step as remaining powders will block the interconnected pores during the sintering step and the permeability of scaffolds for

nutrient transport and waste material removal will be compromised. As a result, the saturation was increased to 75% and stronger green parts were achieved.

The sintered controls and the doped scaffolds are presented in Fig. 3, whereas a report of the designed and sintered pore size along with the compressive strength in MPa is shown in Table 1. The interconnected designed pores were clearly visible from the SEM micrographs. Minimum effective pore sizes reported in the literature for nutrient exchange and proper transport of oxygen necessary for cell survival are around 100  $\mu\text{m}$ , however, a minimum of 200–350  $\mu\text{m}$  interconnected pores are required for osteogenesis and neovascularization. Intending to improve osteogenic and angiogenic properties of the fabricated scaffolds, the designed pore size was fixed at 400  $\mu\text{m}$ . This designed porosity resulted in pore size of 340–350  $\mu\text{m}$  for the TCP scaffolds, 310–330  $\mu\text{m}$  for the Fe-TCP scaffolds and 300–310  $\mu\text{m}$  for the Fe-Si doped scaffolds after sintering.

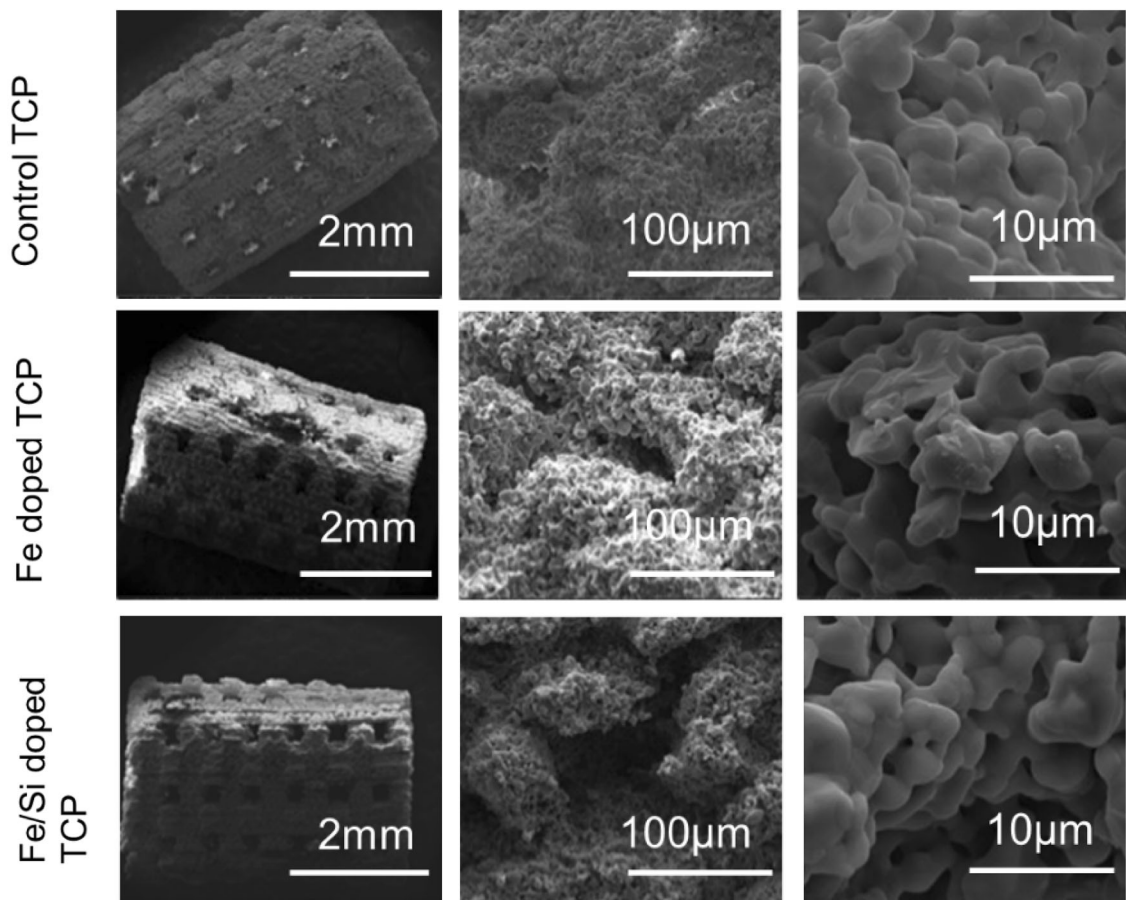


**FIGURE 3.** SEM images of sintered scaffolds and their surface morphology. Interconnected porosity can be clearly seen from the micrographs. Pore sizes were measured as 340–350  $\mu\text{m}$  for the TCP scaffolds, 310–330  $\mu\text{m}$  for the Fe-TCP scaffolds and 300–310  $\mu\text{m}$  for the Fe-Si doped scaffolds after sintering. Micro-porosity is also noted, which were lower in sizes in the doped scaffolds compared to control ones.

**TABLE 1. Volume shrinkage and compressive strength of sintered scaffolds.**

Sample ( $n = 7$ )	Average volume shrinkage after sintering (%)	Compressive strength (MPa)	Pore size after sintering ( $\mu\text{m}$ )
Synthesized TCP	$10.00 \pm 2.1$	$4.9 \pm 0.7$	340–350
Fe doped TCP	$17.89 \pm 0.98$	$17.9 \pm 1.3$	310–330
Fe–Si doped TCP	$16.76 \pm 3.4$	$19.8 \pm 2.4$	300–310

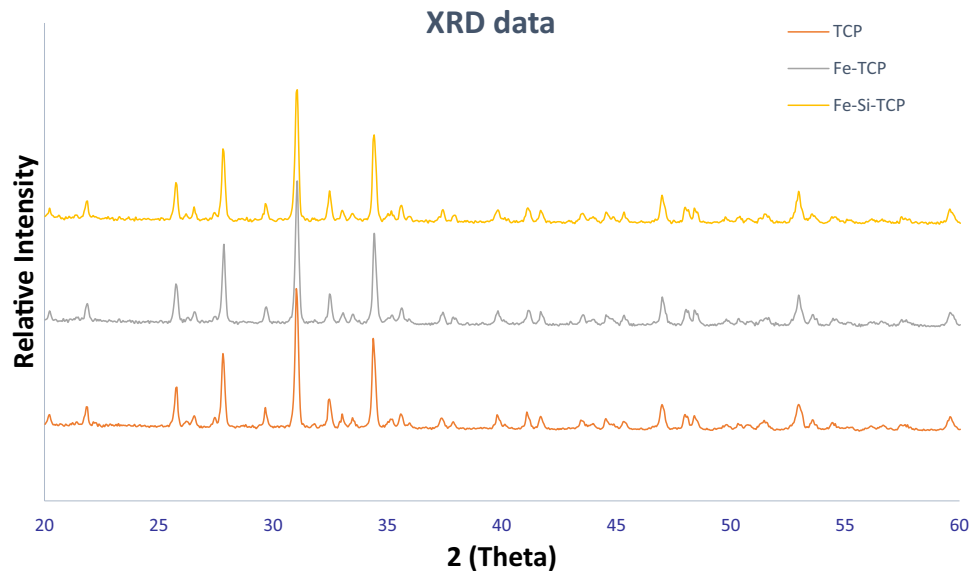


**FIGURE 4. XRD spectra of the doped and the undoped powder. The spectra demonstrate very sharp peaks of  $\beta$ -TCP, dopants were not detected due to the small quantity.**

Figure 4 demonstrates the XRD spectra for the pure TCP, and the doped TCP scaffolds. The XRD peaks received were compared to the JCPDS 09-0169 for  $\beta$ -TCP powder. The sintered  $\beta$ -TCP and doped TCP powder showed no presence of  $\alpha$ -TCP (JCPDS 09-0348), TTCP (JCPDS 25-1137), CaO (JCPDS 82-1691),  $\text{Fe}_2\text{O}_3$ ,  $\text{Fe}_3\text{O}_4$ , and  $\text{SiO}_2$ . The amount of the dopants were too low to be detected in an XRD spectrum. Surface morphologies of the sintered scaffolds were shown in Fig. 3. Other than the designed macro-pores, some residual and intrinsic micropores ( $\sim 20 \mu\text{m}$  in size) were also observed to be uniformly distributed in the sintered scaffolds, which were noted to be lower in size in the doped scaffolds compared to the control TCP scaffolds. This was attributed to the higher densification and smaller grain size in the doped scaffolds compared to the pure TCP ones.

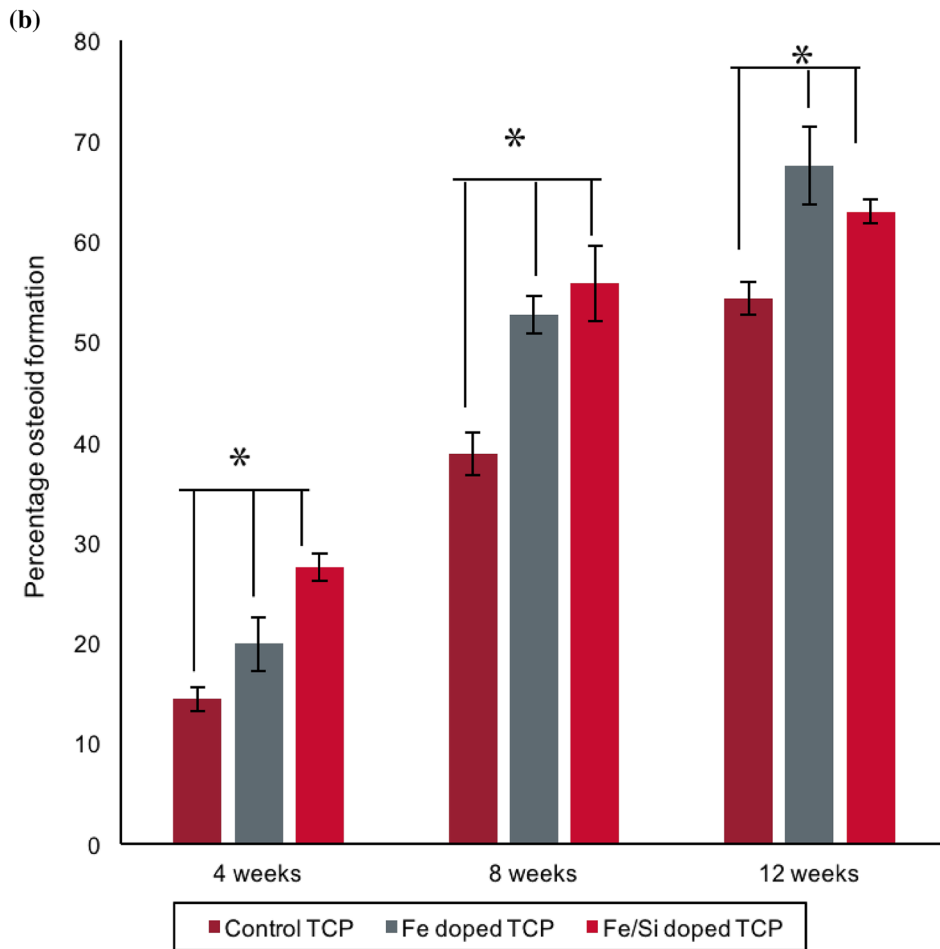
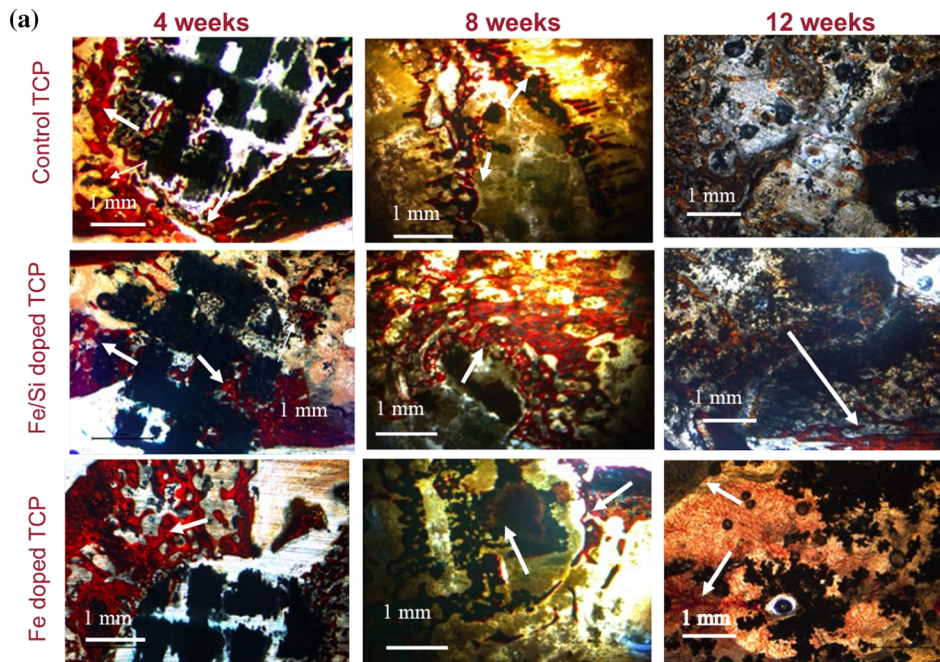
The maximum compressive strength of  $19.8 \pm 2.4$  MPa has been noted in the Fe–Si doped scaffold compared to  $4.9 \pm 0.7$  MPa in the pure TCP scaffolds. The higher strengths in the doped scaffolds were attributed to the higher densification in comparison to the control pure TCP scaffolds.

**FIGURE 5. (a) Osteoid formation by optical microscopy after Modified Masson–Goldner trichrome staining after 4, 8, and 12 weeks for pure and doped TCP scaffolds. Black: implant, orange and red: osteoid, bluish green: mineralized bone. Arrows point out the reddish-orange colors revealing new bone formation. More osteoid formation evident in doped scaffolds compared to control ones. Fe–Si doped scaffolds demonstrate early stage osteoid formation, however, more bone mineralization evident with Fe doping. (b) Histomorphometric analysis performed with Image J software. Doped TCP scaffolds enhance osteoid formation compared to the control ones. Fe–Si doped TCP enhanced early stage osteoid formation up to 8 weeks' time point whereas Fe doped TCP shows better bone mineralization until 12 weeks of implantation [\* shows extremely significant ( $p < 0.05$ ) w.r.t. to control].**

### *In Vivo Study*

#### *Histomorphology and Histomorphometric Analysis*

Histological evaluation was performed to assess the effects of  $\text{Fe}^{+2}$  and  $\text{Si}^{+4}$  on osteoid and new bone formation at 4, 8, and 12 week time points. New bone and mineralized bone was observed at the interface of the implant and the osseous tissue and into the pores of the scaffold, presented in Fig. 5a. The presence of





interconnected porosity facilitated the migration of osteoblast cells into the core of the scaffolds and osteogenesis therein. Figure 5b supports that observation with the histomorphometric analysis performed on the control and doped scaffolds at all time points. More osteoid formation was observed in the doped scaffolds compared to the controls at all time points. Complete mineralization of the new bone into the designed interconnected pores and the micro-pores was noted at the 12-week time point for both the control and doped TCP scaffolds from Fig. 5a. The difference in the new and old osseous tissue formation turned less prominent in the Fe doped at the 12-week time point, which reflected the completed mineralization process. This in turn, also explained the decrease in the osteoid tissue formation by the histomorphometric analysis in Fig. 5b. The enhanced mineralization process in Fe-doped scaffolds also indicated that the presence of Fe in the TCP scaffolds would lead to enhanced bone formation and early stage wound healing when implanted in rat distal femur models. Thus, histological micrographs and histomorphometric calculations revealed that the doped scaffolds facilitated enhanced new bone formation in the early day time points and

improved mineralization in the later stages, indicating potentials for speedy healing.

#### Blood Vessel Staining

New blood vessel formation dictates the functionality of the new tissues formed. Figure 6 shows blood vessel formation inside the scaffolds around the area of implantation, depicted by reddish color. The presence of fully developed blood vessel in the Fe–Si doped scaffolds after 8 and 12 weeks of implants indicated the beneficiary role of the combination of Fe and Si as dopants on the angiogenic factors.

#### Collagen Staining

Expressed by mature osteoblasts, type 1 collagen positively influences the bone mineralization and plays an important role in later stages of bone remodeling. Figure 7 depicts the collagen stained decalcified tissues (brownish red in color) at all time points. At all time-points, the presence of dopants had been noted to enhance collagen formation, rendering more bone mineralization. At week 8 and 12 after necropsy, more collagen formation was

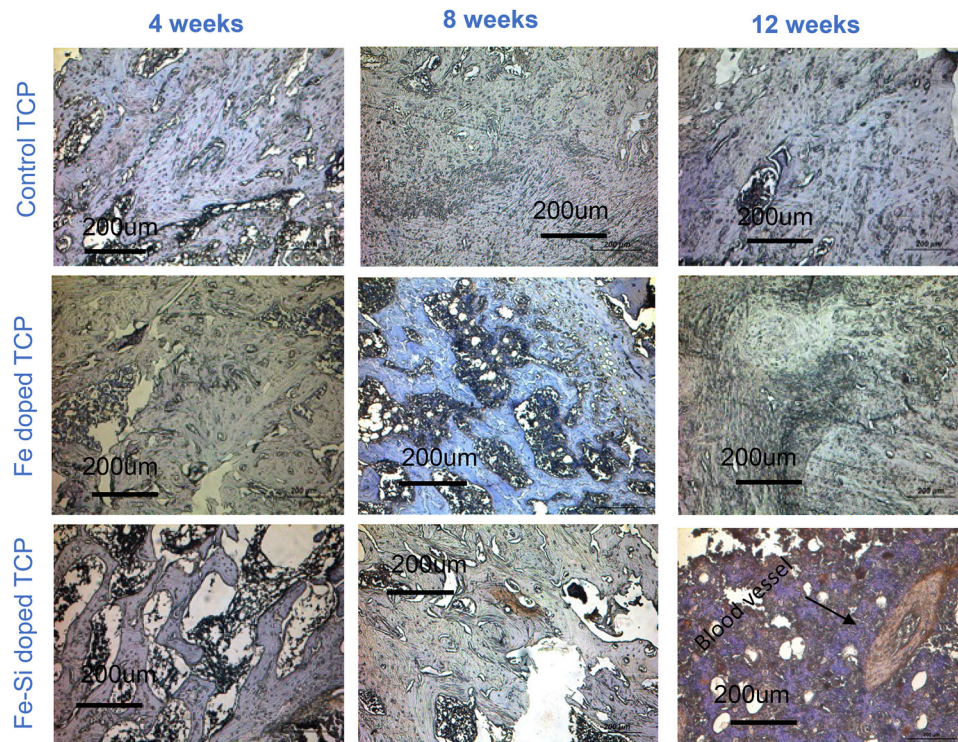


**FIGURE 6.** Blood vessel formation at the implant and host bone interface by VWR staining. Blood vessel has been shown in reddish color and the rest of the tissue stained blue due to hematoxylin counter staining process. Clear evidence of blood vessel formation after 12 weeks in Fe–Si doped scaffolds.



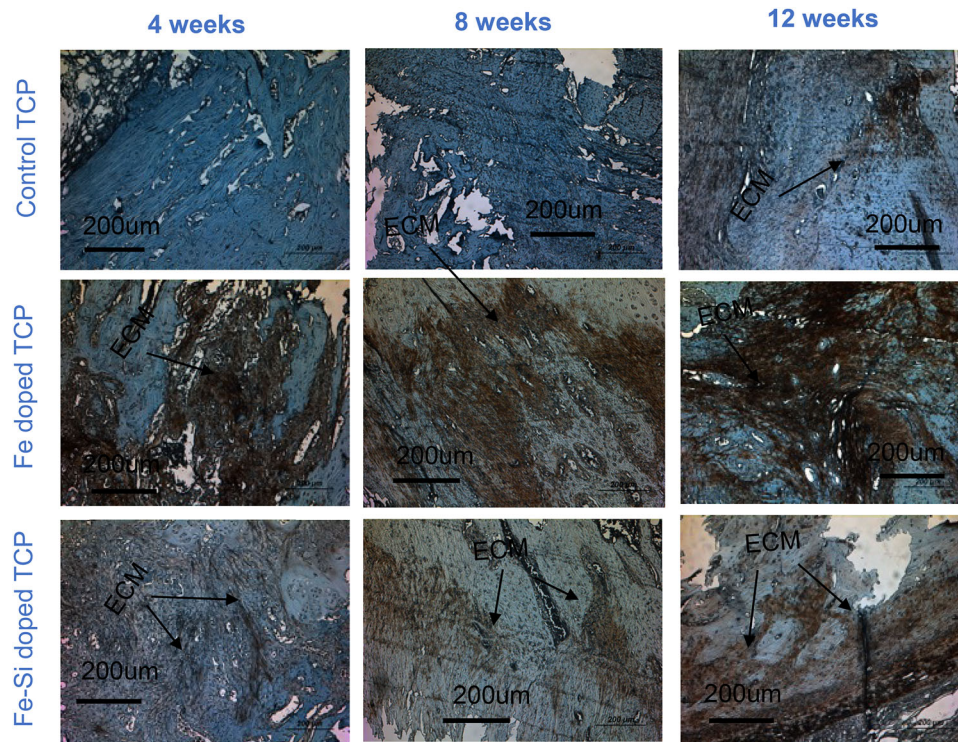


**FIGURE 7.** ECM formation by Type I collagen staining of decalcified samples at the implant and host bone interface. ECM has been shown in reddish-brown color and the rest of the tissue stained blue due to hematoxylin counter staining process. More ECM formation has been seen in Fe-doped scaffolds compared to the control or Fe-Si doped ones.

demonstrated by Fe-doped TCP compared to both Fe-Si doped and control TCP scaffolds and indicated expedited bone mineralization process by the presence of Fe as a dopant. This is also in accordance with the histology micrographs and histomorphometric analysis results reported before. The enhancement of collagen I formation by the presence of Fe demonstrated the influence of Fe in the rapid bone remodeling and, improved defect healing.

#### *Hematoxylin and Eosin Staining*

DNA and RNA of the cells present in the nucleus and some RNA, anchored on the rough endoplasmic reticulum are acidic molecules as they are made up of a huge negatively charged phosphate backbone. These huge biomolecules react with basic dyes like hematoxylin (dark blue/violet stain) to form salts and stain violet. In turn, the basic constituents of the cell like most proteins of the cytoplasm, intracellular and extracellular membranes stain pink with eosin. The erythrocytes stain the darkest. Pure TCP and doped TCP scaffolds induced bone formation and were stained by H&E staining as depicted in Fig. 8. New bone formation was observed inside the micropores and macropores of the control and doped scaffolds. Dark reddish pink stain was noted in the Fe-Si doped

scaffolds around the area of implantation, mostly after 8 and 12-week time points, indicating the induction of blood vessels formation by the combined presence of  $\text{Fe}^{+3}$  and  $\text{Si}^{+4}$ . These results collate our findings from the vWF staining process.

## DISCUSSION

One of the primary objectives of resorbable bone implants is to provide the necessary mechanical strength to maintain the original shape and structural function of the removed tissue throughout the effective lifetime of the implants. The implant must be able to withstand typical mechanical stresses until the bone tissue has repaired to the point of off-loading the implant. The favorable solubility constant of  $\beta$ -TCP ensures a rate of dissolution in the body that is similar to the growth rate of bone, thus its use in scaffolds. Powder quality is crucial to controlling solubility and the sintering properties which will determine the scaffold's mechanical strength. Previous studies of scaffold fabrication using 3D printing utilized commercially pure powder. The synthesized powder in this study resulted in pure  $\beta$ -TCP and well-incorporated dopants that significantly increased densification and improved mechanical strength of the scaffolds. Secondly, the

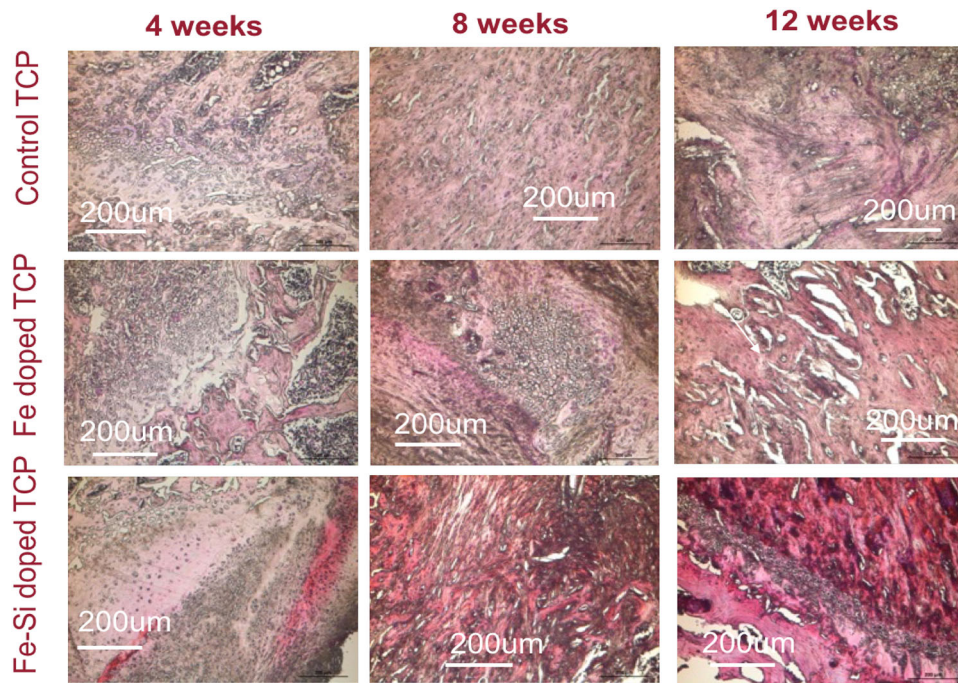


**FIGURE 8.** Histological decalcified specimen of rat distal femur by H&E staining. In the optical microscopy, nuclei can be observed in blue/purple, basophils in purplish red, erythrocytes in cherry red, collagen and osteoid tissues in a variety of pink shades. Enhancement of cherry red color in Fe–Si doped scaffolds after 12 weeks shows incorporation of erythrocytes around the area of implantation.

implant should act as a scaffold to support bone growth along and within the implant itself. Density, pore size, microstructure, phase, and mechanical strength are important parameters that can dictate implant outcomes *in vivo*.

Pore size positively impacts the new bone formation by enhancing the tissue in growth and improving vascularization, but negatively influences the mechanical properties of the scaffolds. Minimum effective pore sizes reported in the literature for nutrient exchange and proper transport of oxygen necessary for cell survival are around 100  $\mu\text{m}$ , although a minimum of 200–350  $\mu\text{m}$  interconnected porosity is required for osteogenesis and neo vascularization,<sup>31</sup> with optimal ingrowth occurring in the 300–500  $\mu\text{m}$  range.<sup>16,25</sup> To account for shrinkage during sintering, a designed pore size of 400  $\mu\text{m}$  resulted in pore diameters of pure, Fe, and Fe–Si scaffolds that measured 340–350, 310–330, and 300–310  $\mu\text{m}$ , respectively. The addition of Fe and Fe–Si each enhanced the densification of TCP, which is further confirmed by average volume shrinkages of 17.89, 16.76, and 10.00% for Fe-doped, Fe–Si-doped, and pure samples, respectively. Increased densification may be due to the presence of the  $\text{Fe}_2\text{O}_3$  during milling and sintering, which can lead to the formation of CHA by substitution of the  $\text{Fe}^{3+}$  ions into the  $\text{Ca}^{2+}$  lattice sites<sup>20</sup>; similar substitution can occur for TCP resulting

in decreased crystallinity. This decrease in crystallinity can decrease the melting point of TCP, allowing for greater densification at the same sintering temperature. Conversely, the addition of  $\text{SiO}_2$  may have prevented further densification of the Fe–Si-doped scaffolds due to its higher melting point (1710  $^\circ\text{C}$ ) and the relatively low sintering temperature. This conclusion is further supported by the previous study of Si–HA systems that showed a decreased densification with increased silicon content at a sintering temperature of 1000–1150  $^\circ\text{C}$ .<sup>4</sup>

Despite a smaller measured volume of shrinkage than Fe-TCP, Fe–Si-TCP scaffolds displayed higher compressive strengths. Strength values of  $4.9 \pm 0.7$ ,  $17.9 \pm 1.3$ , and  $19.8 \pm 0.4$  MPa were measured for pure, Fe-TCP, and Fe–Si-TCP. Similar increases in the compressive strength of TCP have been reported, although the rise in strength was associated with increased density.<sup>28</sup> Increased strength may have been achieved due to the reduced macro-pore size, putting the load-bearing struts in closer proximity to each other, even though the scaffolds' average volume shrinkage was less than Fe-TCP. The compressive strength of human mandibles also has been reported to range from 0.22 to 10.44 MPa in nine freshly frozen human mandibles from an age of 56–90 years.<sup>24</sup> The compressive strengths of the 3D printed porous doped TCP scaffolds fabricated in this study ranged from 4.2



to 23.2 MPa. Therefore, we believe that these scaffolds would be able to withstand the physiological loads experienced in craniomaxillofacial applications.

The modified Masson–Goldner-staining shown in Fig. 5a was used to determine the degree of new bone (osteoid) formation, mineralization of the osteoid into mature bone, and implant resorption. At the 4-week time point, the scaffolds were clearly visible with some degree of osteoid development within the designed pores of all three compositions. Osteoid proximity to the outer surface of the scaffold was nearer in Fe-TCP and Fe–Si-TCP than pure TCP from a qualitative standpoint. Degradation of the scaffold at week 8 had progressed from the earlier time point with large pores seen in Fe-TCP scaffolds and a greatly reduced cross-section in Fe–Si-TCP scaffolds. Although faint, darker colored cross-sections of the pure TCP struts could still be seen around the osteoid. Large pockets of osteoid were present within the Fe-TCP, and the Fe–Si scaffolds were integrated with large bodies of new bone. At 12 weeks, the scaffolds were difficult to discern within the tissue samples and appear to have fragmented into granules best illustrated in the Fe-TCP image. While the Fe-TCP samples showed more apparent osteoid than Fe–Si-TCP, the Fe–Si-TCP samples appeared to contain more mineralized bone at the implant site. Although both osteoid and mineralized bone were present in the tissue surrounding the pure TCP scaffolds, only partial replacement of the center of the scaffold with mineralized bone occurred. Corroborating the qualitative assessment, the histomorphometric analysis in Fig. 5b showed a significantly higher amount of osteoid formation due to the presence of dopants at all time points. The relatively smaller percentage of osteoid in the Fe–Si-TCP samples compared to Fe-TCP at 12 weeks may be due to the maturation of the osteoid into mineralized bone as seen in the stained images.

Recruitment of blood vessels to the injury site is crucial for expediting the wound healing process and providing proper oxygenation to promote osteoblastogenesis. Additionally, blood vessel formation is critical to the survival of cells located at the center of porous scaffolds as diffusion-based nutrient transport, which dominates areas of low vascularization, is not sufficient to support the cells. Cells located in the center can experience oxygen tension and poor nutrient supply as those located on the outer edges of the scaffold consume these metabolites. vWF is secreted by endothelial cells, and its presence in the wound indicates their recruitment from nearby vessels. Figure 6 shows vWF staining of demineralized tissue samples, where no noticeable staining occurred for both pure and Fe-TCP samples at all time points. Fe–Si-TCP samples showed some degree of staining at week 8, and at week 12 fully developed blood vessels could be seen

within the wound area. The role of silicon in promoting angiogenesis is dramatic in this figure as only Fe–Si-TCP samples showed any positive staining.  $\text{Si}^{4+}$  is thought to enhance angiogenesis through the activation and promotion of vascular endothelial growth factor (VEGF), which further upregulates nitric oxide (NO) production.<sup>23</sup> NO acts on endothelial cells, increasing proliferation, migration and cellular adherence to the surrounding extracellular matrix.<sup>23</sup> This further elucidates the necessity of multiple dopants as Fe doped scaffolds had no noticeable effect on vascularization compared to pure TCP.

Furthermore, iron plays a very crucial role in many enzymatic reactions in the body, including the ones involving collagen biosynthesis. Assembly of three dimensional strands, with glycine and lysine as principle components forms procollagen which later glycosylates and forms the triple helical collagen.<sup>12</sup>  $\text{Fe}^{3+}$  is reduced to its active state of  $\text{Fe}^{2+}$  by ascorbate for the assembly of three dimensional stands forming procollagen<sup>6</sup> and thus, plays a crucial role in collagen formation. Type I collagen is the most abundantly found protein in animals, and more than 90% of bone protein constitutes of collagen.<sup>27</sup> Also, collagen is the main constituent of the organic material present in bone, as well as a major matrix protein found in the ECM. Enhanced type I collagen production can promote the formation of boney callus, stabilizing the wound prior to remodeling, as well as increase osteoid production.<sup>10</sup> At both 4 and 12-week time points, the presence of type I collagen was greatly increased in Fe- and Fe–Si-TCP compared to pure TCP, which showed no noticeable amount of type I collagen at 4 weeks, seen in Fig. 7. It has been shown that  $\text{Fe}^{2+}$  plays a role in the formation of type I collagen during the hydroxylation stage of procollagen and is created through the reduction of  $\text{Fe}^{3+}$  by ascorbate.<sup>10</sup> In addition, the previous study of  $\text{SiO}_2$  in TCP scaffolds reported that the presence of  $\text{Si}^{4+}$  may enhance type I collagen production.<sup>14</sup> Greater amounts of type I collagen at early time points suggested enhanced ECM formation near the wound which would act as a stabilizer, reducing strain and initiating osteoblast recruitment thereby increasing osteoid formation and mineralization. This was further corroborated by Figs. 5a and 5b where greater osteoid formation at early time points (weeks 4 and 8) was seen in Fe–Si doped scaffolds.

To better observe the cellular bodies present in the decalcified samples, H&E staining was used to stain basophilic cellular entities blue and eosinophilic entities pink or red. Magnified images taken within the wound areas are shown in Fig. 8. Week 4 tissue slides for pure TCP showed considerable amounts of granuloma tissue with some osteoid formation, while Fe-TCP and Fe–Si-TCP both showed large areas of osteoid formation around the wound. At week 8 the



tissues surrounding all three compositions were largely comprised of non-woven bone, and adipocytes appeared to be present in the center of the week 8 Fe-TCP image. Tissue morphology at the 12-week time point showed that pure TCP samples were still mostly woven bone, however, Fe-TCP samples showed more mature spongy bone formation and Fe-Si-TCP samples showed well developed trabecular bone and spongy bone separated by a layer of osteoblasts. It was noted that the Fe-Si-TCP samples stained a much deeper red than the other samples, which may indicate greater vascularization through the presence of erythrocytes, which are highly eosinophilic.

After optimization of a variety of parameters for powder bed 3D printing including layer thickness, drop volume, binder volume, saturation, and drying and heating rates, Fe<sup>+3</sup> and Si<sup>+4</sup> doped  $\beta$ -TCP scaffolds with interconnected designed porosity of 400  $\mu$ m were able to be fabricated. The objective of this study was to analyze the effects of interconnected porosity and dopants on the mechanical properties of the 3D printed scaffolds and early and late stage osteogenesis and angiogenesis *in vivo*. Undoped, Fe and Fe-Si-doped scaffolds showed compressive strengths of  $4.9 \pm 0.7$ ,  $17.9 \pm 1.3$  and  $19.8 \pm 2.4$  MPa respectively, revealing that the presence of dopants led to better densification and hence, improved mechanical strengths after sintering. The presence of Fe was observed to enhance bone mineralization around the area of implantation, whereas the presence of Si with Fe improved early stage osteoid formation, evident from the modified Masson-Goldner-staining. Fe and Fe-Si doped scaffolds improved the early stage osteoconduction, by the stabilization of the implant through enhanced ECM development, evidenced by the increased amount of type 1 collagen formation in the surrounding tissue. The presence of Si<sup>+4</sup> along with Fe<sup>+3</sup> in the TCP scaffolds led to neovascularization between 8 and 12 weeks of implantation, which is crucial for improving waste removal from, and nutrient delivery to the internal pores of the scaffolds improving healing throughout the wound. These findings suggest that the combined presence of Fe and Si dopants in 3D printed scaffolds with interconnected porosity is an excellent system for introducing osteogenic and angiogenic properties, and thus suitable for bone tissue engineering applications.

#### ACKNOWLEDGMENTS

Authors would like to acknowledge financial support from the National Institutes of Health under Grant Numbers R01 AR066361 and do not have any

possible conflict of interest. The authors would like to acknowledge help from Valerie Lynch-Holm and Dan Mullendore from Franceschi Microscopy & Imaging Center (FMIC), WSU and Washington Animal Disease Diagnostic Lab (WADDL) with the *in vivo* staining procedures. The content is solely the responsibility of the authors and does not necessarily represent the official views of the National Institute of Health.

#### REFERENCES

- <sup>1</sup>ASTM C773-88. Standard test method for compressive (crushing) strength of fired whiteware materials. ASTM International, West Conshohocken, PA, 2016. [www.astm.org](http://www.astm.org).
- <sup>2</sup>Bandyopadhyay, A., S. Bernard, W. Xue, and S. Bose. Calcium phosphate-based resorbable ceramics: influence of MgO, ZnO, and SiO<sub>2</sub> dopants. *J. Am. Ceram. Soc.* 89(9):2675–2688, 2006.
- <sup>3</sup>Becker, S. T., P. H. Warnke, E. Behrens, and J. Wiltfang. Morbidity after iliac crest bone graft harvesting over an anterior versus posterior approach. *J. Oral Maxillofac. Surg.* 69(1):48–53, 2011.
- <sup>4</sup>Bose, S., D. Banerjee, and A. Bandyopadhyay. Introduction to biomaterials and devices for bone disorders. *Mater. Bone Disord.* 2017. <https://doi.org/10.1016/B978-0-12-802792-9.00001-X>.
- <sup>5</sup>Bose, S., M. Roy, and A. Bandyopadhyay. Recent advances in bone tissue engineering scaffolds. *Trends Biotechnol.* 30(10):546–554, 2012.
- <sup>6</sup>de Jong, L., and A. Kemp. Stoichiometry and kinetics of the prolyl 4-hydroxylase partial reaction. *Biochim. Biophys. Acta* 787(1):105–111, 1984.
- <sup>7</sup>Fielding, G. A., A. Bandyopadhyay, and S. Bose. Effects of silica and zinc oxide doping on mechanical and biological properties of 3D printed tricalcium phosphate tissue engineering scaffolds. *Dent. Mater.* 28(2):113–122, 2012.
- <sup>8</sup>Fielding, G., and S. Bose. SiO<sub>2</sub> and ZnO dopants in three-dimensionally printed tricalcium phosphate bone tissue engineering scaffolds enhance osteogenesis and angiogenesis *in vivo*. *Acta Biomater.* 9(11):9137–9148, 2013.
- <sup>9</sup>Forth, W., and W. Rummel. Iron absorption. *Physiol. Rev.* 53(3):724–792, 1973.
- <sup>10</sup>Glatt, V., C. H. Evans, and K. Tetsworth. A concert between biology and biomechanics: the influence of the mechanical environment on bone healing. *Front. Physiol.* 7:678, 2017.
- <sup>11</sup>Goldberg, V. M. Natural history of autografts and allografts. In: Bone implant grafting, edited by M. W. J. Older. London: Springer, 1992, pp. 9–12.
- <sup>12</sup>Gorres, K. L., and R. T. Raines. Prolyl 4-hydroxylase. *Crit. Rev. Biochem. Mol. Biol.* 45(2):106–124, 2010.
- <sup>13</sup>Jones, A. C., C. H. Arns, D. W. Hutmacher, B. K. Milthorpe, A. P. Sheppard, and M. A. Knackstedt. The correlation of pore morphology, interconnectivity and physical properties of 3D ceramic scaffolds with bone ingrowth. *Biomaterials* 30(7):1440–1451, 2009.
- <sup>14</sup>Jugdaohsingh, R. Silicon and bone health. *J. Nutr. Health Aging* 11(2):99, 2007.

- <sup>15</sup>Kannan, S., A. F. Lemos, J. H. Rocha, and J. M. Ferreira. Characterization and mechanical performance of the Mg-stabilized  $\beta$ - $\text{Ca}_3(\text{PO}_4)_2$  prepared from Mg-substituted Ca-deficient apatite. *J. Am. Ceram. Soc.* 89(9):2757–2761, 2006.
- <sup>16</sup>Karageorgiou, V., and D. Kaplan. Porosity of 3D biomaterial scaffolds and osteogenesis. *Biomaterials* 26(27):5474–5491, 2005.
- <sup>17</sup>Katsumata, S. I., R. Katsumata-Tsuboi, M. Uehara, and K. Suzuki. Severe iron deficiency decreases both bone formation and bone resorption in rats. *J. Nutr.* 139(2):238–243, 2009.
- <sup>18</sup>Katsumata, S. I., R. Tsuboi, M. Uehara, and K. Suzuki. Dietary iron deficiency decreases serum osteocalcin concentration and bone mineral density in rats. *Biosci. Biotechnol. Biochem.* 70(10):2547–2550, 2006.
- <sup>19</sup>Khalyfa, A., S. Vogt, J. Weisser, G. Grimm, A. Rechtenbach, W. Meyer, and M. Schnabelrauch. Development of a new calcium phosphate powder-binder system for the 3D printing of patient specific implants. *J. Mater. Sci. Mater. Med.* 18(5):909–916, 2007.
- <sup>20</sup>Li, Y., C. T. Nam, and C. P. Ooi. Iron (III) and manganese (II) substituted hydroxyapatite nanoparticles: characterization and cytotoxicity analysis. *J. Phys.* 187:012024, 2009.
- <sup>21</sup>McGillivray, G., S. A. Skull, G. Davie, S. E. Kofoed, A. Frydenberg, J. Rice, *et al.* High prevalence of asymptomatic vitamin D and iron deficiency in East African immigrant children and adolescents living in a temperate climate. *Arch. Dis. Child.* 92(12):1088–1093, 2007.
- <sup>22</sup>Medeiros, D. M., A. Plattner, D. Jennings, and B. Stoecker. Bone morphology, strength and density are compromised in iron-deficient rats and exacerbated by calcium restriction. *J. Nutr.* 132(10):3135–3141, 2002.
- <sup>23</sup>Miller, T. W., J. S. Isenberg, and D. D. Roberts. Molecular regulation of tumor angiogenesis and perfusion via redox signaling. *Chem. Rev.* 109(7):3099–3124, 2009.
- <sup>24</sup>Misch, C. E., Z. Qu, and M. W. Bidez. Mechanical properties of trabecular bone in the human mandible: implications for dental implant treatment planning and surgical placement. *J. Oral Maxillofac. Surg.* 57(6):700–706, 1999.
- <sup>25</sup>Otsuki, B., M. Takemoto, S. Fujibayashi, M. Neo, T. Kokubo, and T. Nakamura. Pore throat size and connectivity determine bone and tissue ingrowth into porous implants: three-dimensional micro-CT based structural analyses of porous bioactive titanium implants. *Biomaterials* 27(35):5892–5900, 2006.
- <sup>26</sup>Price, C. T., K. J. Koval, and J. R. Langford. Silicon: a review of its potential role in the prevention and treatment of postmenopausal osteoporosis. *Int. J. Endocrinol.* 2013. <https://doi.org/10.1155/2013/316783>.
- <sup>27</sup>Proff, P., and P. Römer. The molecular mechanism behind bone remodelling: a review. *Clin. Oral Invest.* 13(4):355–362, 2009.
- <sup>28</sup>Tang, R., W. Wu, M. Haas, and G. H. Nancollas. Kinetics of dissolution of  $\beta$ -tricalcium phosphate. *Langmuir* 17(11):3480–3485, 2001.
- <sup>29</sup>Tarafder, S., V. K. Balla, N. M. Davies, A. Bandyopadhyay, and S. Bose. Microwave-sintered 3D printed tricalcium phosphate scaffolds for bone tissue engineering. *J. Tissue Eng. Regen. Med.* 7(8):631–641, 2013.
- <sup>30</sup>Tarafder, S., N. M. Davies, A. Bandyopadhyay, and S. Bose. 3D printed tricalcium phosphate bone tissue engineering scaffolds: effect of SrO and MgO doping on in vivo osteogenesis in a rat distal femoral defect model. *Biomater. Sci.* 1(12):1250–1259, 2013.
- <sup>31</sup>Vahabzadeh, S., and S. Bose. Effects of iron on physical and mechanical properties, and osteoblast cell interaction in  $\beta$ -tricalcium phosphate. *Ann. Biomed. Eng.* 45(3):819–828, 2017.
- <sup>32</sup>Yang, S., K. F. Leong, Z. Du, and C. K. Chua. The design of scaffolds for use in tissue engineering. Part II. Rapid prototyping techniques. *Tissue Eng.* 8(1):1–11, 2002.
- <sup>33</sup>Zhang, M., and H. Ramay. U.S. Patent Application No. 10/846,356, 2005.